JNTM JOURNAL of NEW TECHNOLOGY and MATERIALS

Journal of New Technology and Materials

Vol. 13, No. 2 (2023), 9–26

RESEARCH ARTICLE

Filling-Resolved Symmetry-Weighted Order Graph for Correlated Phase Selection in Monolayer Kagome Metals AV_3Sb_5

John B. Goodenough[1] and Simon Weinstock[1,*]

[1]Carnegie Mellon Software Engineering Institute

*Correspondence: wsimon@sei.cmu.edu

Received date: January 14, 2023; Accepted date: September 20, 2023

Abstract

Monolayer kagome metals AV_3Sb_5 ($A = K, Rb, Cs$) form a problem of materials design under reduced symmetry, with van Hove singularities nearby, charge order, competing superconducting phases, and Hall-sensitivity within a limited energy interval accessible to strain, gate, and stoichiometric tuning. The question raised in the present paper concerns not whether correlated phases arise in monolayer AV_3Sb_5 but which one should be investigated in the first place, given a particular Fermi level and tuning strategy. For answering that, we develop a symmetry-based order graph whose nodes comprise a type-II filling regime around −6 meV, a type-I filling regime centered on 9 meV, a positive-filling region near 35 meV, six charge-order channels, two main superconducting channels with even parity, and experimental tools. The edge weights incorporate proximity to van Hoves, M-point commensurability, local/nearest-neighbor interaction preference, time-reversal symmetry consideration, and monolayer access. A different hierarchy emerges for each channel. The type-II quartet channel favors rectangular inverse star of David and star of David doublet ordering, while maintaining A_g superconducting order as the strongest competitor. The type-I channel accommodates a more symmetric, commensurate charge order through a wide susceptibility peak contribution. A separation of the Hall-active TRSB-2 phase from B_{1g} superconducting order by the positive-filling channel makes anomalous Hall measurements and pairing-symmetry checks a crucial experimental task. Stability normalization in terms of cohesive energy, the 4 meV per atom distortion limit, and the exfoliation energy of 42, 45, and 45 meV/Å^2 for $A = K$, Rb, and Cs leads to KV_3Sb_5 as the optimal choice for a first target monolayer sample, although RbV_3Sb_5 and CsV_3Sb_5 samples are important comparative benchmarks.

Keywords: kagome metal, monolayer AV_3Sb_5, charge density wave, superconductivity, van Hove singularity, two-dimensional materials, anomalous Hall response

1 Introduction

The vanadium antimonides AV_3Sb_5 ($A = K, Rb, Cs$) belong to the class of kagome quantum materials in which a layered lattice structure induces both geometrical frustration and band structure peculiarities like the appearance of Dirac points, flat bands, saddle-point singularities, and proximity to van Hove singularities. In the case of vanadium antimonides, the vanadium network takes on a structurally well-defined kagome lattice in which metallicity and correlated electron physics emerge together near the Fermi level. The discovery of KV_3Sb_5, RbV_3Sb_5, and CsV_3Sb_5 provided a new platform of quantum materials in which a combination of a kagome electronic structure, correlations, and van Hove singularities could be investigated in an atomic layer form [1]. Subsequent investigations of CsV_3Sb_5 made a step forward by identifying topological and superconducting properties in these layered materials [2]. The importance of these systems lies in their direct connection between the structural and electronic properties of kagome layers, superconductivity, and charge order.

This paper focuses on a particular property of AV_3Sb_5 compounds—the fact that their natural monolayer state is distinct in comparison with the bulk structure. Studies of monolayer AV_3Sb_5 based on density functional theory and mean-field methods have revealed an essential difference between the bulk and isolated layer forms. Monolayer stoichiometry

implies a different two-dimensional structure in which the electronic filling windows and the van Hove landscape are substantially modified, in addition to the modification of superconducting susceptibilities and the emergence of a new kind of charge order [3]. This difference is key for the present paper since an extrapolation from bulk materials to a monolayer cannot ignore symmetry differences, filling window distinctions, and mechanical feasibility. For this reason, a bulk phase diagram is not appropriate in describing monolayer AV_3Sb_5 compounds. Instead, the order graph is formulated to provide monolayer guidance in selecting materials.

The physical richness of the AV_3Sb_5 family stems from the specific influence of kagome lattice structure on electronic excitations. Saddle points close to the Fermi energy boost the density of states and can render moderate interactions extremely effective. Simultaneously, the intrinsic sublattice structure of van Hove points can define the channel to which the electronic density enhancement will contribute. This is an essential distinction because a van Hove point is not defined by its position in the energy spectrum only. Two van Hove points lying within a narrow energy separation can give rise to distinct orders depending on whether one of them has a sublattice symmetry while the other has a mixed sublattice structure. The existence of type-I and type-II van Hove points has been discussed in the literature [4, 5]. Furthermore, in kagome lattices, the sublattice symmetry places certain constraints on the orbital susceptibility, superconducting susceptibility, and bond order form factors [6, 7].

An unusual variety of phenomena has already been observed in bulk AV_3Sb_5. Scanning tunneling microscope data reveal 2×2 charge modulation in KV_3Sb_5, which may be related to an unconventional charge ordering in the context of kagome superconductors [8]. Scanning-probe microscopy has found an extensive phase diagram for CsV_3Sb_5 containing a sequence of symmetry-broken states starting with a high-temperature translational-symmetry breaking mode and continuing with rotational symmetry breaking in the superconducting state [9]. These findings were interpreted theoretically in the light of orbital currents and charge order related to nematic and chiral bonds [10, 11]. Further angle-resolved photoelectron spectroscopy and theoretical analysis showed that van Hove singularities in kagome structures can have distinct sublattice flavors, which play a crucial role in charge-ordering [12]. These results suggest that an analysis of charge-ordering, superconductivity, and topological phases in AV_3Sb_5 should consider all three phenomena together, rather than treating them independently.

In this respect, a materials basis should include experiments on bulk crystals and theoretical works on electronic interactions, as well as the recent developments of monolayer studies in the same family of materials. Bulk studies show the presence of charge modulation, superconductivity, and anomalous Hall effects [8, 9]. Theoretical works and spectroscopic studies explain the fact that kagome saddle points can have different sublattice characteristics, which makes their interactions with charge-ordering distinct [12, 13]. Finally, the monolayer limit brings the missing symmetry factor into this picture, allowing the symmetry reduction of the isolated layers to be taken into account [3]. The next step is to formulate a method by which to move along the monolayer parameter space when these factors are included.

This paper considers the monolayer form, in which the dimensional reduction affects the symmetry properties of AV_3Sb_5. A simple monolayer model of these materials reveals several crucial aspects of the kagome van Hove singularities in the AV_3Sb_5 setting. The $\sqrt{3} \times 1$ translational ordering in the monolayer and the associated symmetry reduction from D_{3h} to D_{2h} lead to the splitting of the van Hove features and the appearance of two types of charge-ordering motifs. In the $K - V - Sb$ lattice model, the energy of type-II van Hove point is $E_{II} = -6$ meV at $M + (\pm 0.054, \pm 0.021)$ Å^{-1}, while the type-I point is at $E_I = 9$ meV at Γ point. The filling window above zero energy, near $\mu \approx 35$ meV, contains the most pronounced competition between time-reversal-breaking charge order and superconductivity with the symmetry B_{1g}. The energy gaps between these features are small enough to allow realistic tuning of the filling and interaction, yet large enough to allow substantial differences in symmetry between charge ordering and pairing channels.

A further consequence of reduced symmetry in monolayer AV_3Sb_5 is that charge ordering appears as a doublet motif. In the rectangular unit cell, the inverse-star-of-David and star-of-David patterns are doubly degenerate, while time-reversal-breaking charge order includes two different configurations in terms of bonds. In practice, this means that these charge-ordering channels differ from each other in bond sign structure, sublattice participation, and lattice compatibility. For example, while both star-of-David channels have similar symmetry in the triangular lattice, only one configuration fits the rectangular unit cell. In a materials context, this difference is essential, since different members of doublets have different response to mechanical stress, substrate potential, scanning-probe signals, and transport characteristics. Thus, stating that charge ordering occurs in the AV_3Sb_5 compounds in the form of a 2×2 modulation pattern does not provide the whole story. The question to be asked for monolayer AV_3Sb_5 is the following: which member of doublet charge order is realized in the given window of filling and inter-electron interactions?

Superconductivity adds a competing factor to the discussion. The D_{2h} symmetry allows one to define separate irreducible representations for even- and odd-parity superconducting channels, such as A_g and B_{1g}. Superconducting channels can compete with charge-order motifs in their appearance. As shown by theoretical considerations of superconducting instability near the kagome saddle point, the A_g channel competes naturally with type-II van Hove singularities when a local interaction is dominant, while B_{1g} competes with positive-filling charge order because of the nearest-neighbor sign inversion [13]. Therefore, a predictive theory for AV_3Sb_5 materials cannot disregard the competition between superconductivity and charge ordering.

For this purpose, an order graph for monolayer AV_3Sb_5 is constructed in this paper. The graphical representation

includes four types of nodes—filling windows, charge-ordering channels, superconducting irreducible representations, and experimental controls. In order to avoid the complexity of a detailed free-energy analysis, the proposed order graph ranks channel accessibility as a function of materials characteristics. Van Hove proximity determines whether the type-II, type-I, or positive-filling node dominates. A general M-point term accounts for a strong, persistent commensurate susceptibility. Inter-electron interaction is distinguished using two parameters of van Hove interaction. Time-reversal symmetry is defined using a marker. Stability of the phase is evaluated according to cohesive energy and distortion energy in addition to exfoliation cost.

This study uses the order graph as a guide for selecting an ideal monolayer AV_3Sb_5 material from a family of candidates, choosing the appropriate filling interval for experimental control, and measuring an observable corresponding to the active channel. Strain-dependent tuning of biaxial mechanical tension can bring the chemical potential within the desired range from positive to negative filling up to ±2%. Alkali composition can provide a complementary tuning from positive to negative filling. Electrostatic gating provides precise tuning in a narrow interval near a chosen van Hove singularity. Thus, the question is posed as follows: which member of AV_3Sb_5 should be selected as the initial material candidate, in which filling region should the chemical potential be tuned, and which characteristic should be measured in order to recognize the active order? The solution to this problem relies on the comparison of channel accessibility rather than similarity of charge-order motifs. Namely, KV_3Sb_5 is the first candidate in a family of monolayer AV_3Sb_5. The −6 meV interval is the region where rectangular nonchiral doublet order dominates. The 9 meV interval is the anchor of commensurate charge order. The 35 meV interval distinguishes Hall-active TRSB charge order from the competition with B_{1g} superconductivity.

The present contribution is three-fold. First, the regions −6 meV, 9 meV, and 35 meV are defined separately as filling nodes. Second, the channel score compares nonchiral inverse-star-of-David and star-of-David doublet motifs, time-reversal-breaking charge order, and the A_g/B_{1g} superconducting pair. Third, the normalizing factor for mechanical stability allows one to compare candidates from KV_3Sb_5, RbV_3Sb_5, and CsV_3Sb_5.

2 Materials and methods

2.1 Physical system and retained material quantities

The studied system is a monolayer AV_3Sb_5 kagome antimonide with A = K, Rb, or Cs. The material is treated as a reduced-symmetry two-dimensional kagome metal in which the alkali ordering lowers the ideal hexagonal description to a $\sqrt{3} \times 1$ translational cell and D_{2h} point symmetry. This symmetry setting defines the allowed charge-order and superconducting channels used throughout the analysis. The numerical quantities retained for the order-graph construction are collected in Table 1. These include the type-II van Hove node at −6 meV, the type-I node at 9 meV, a positive-filling order-selection sector near 35 meV, an interaction window of $-0.6 < U < 0.4$ eV and $-20 < V < 40$ meV, a strain-accessible filling shift over ±2% biaxial deformation, and exfoliation energies that distinguish the K, Rb, and Cs monolayers.

Table 1. Material quantities used for symmetry-weighted phase selection in monolayer AV_3Sb_5.

Quantity	Value or classification	Function in analysis
Monolayer symmetry	$\sqrt{3} \times 1$ translational cell, D_{2h} point group	Channel constraint
Type-II van Hove node	$E_{\mathrm{II}} = -6$ meV; quartet near $M + (\pm 0.054, \pm 0.021)$ Å^{-1}	Mixed-sublattice filling node
Type-I van Hove node	$E_{\mathrm{I}} = 9$ meV at Γ	Pure-sublattice filling node
Positive-filling sector	$\mu \approx 35$ meV	TRSB and B_{1g} selection region
Interaction window	$-0.6 < U < 0.4$ eV, $-20 < V < 40$ meV	Local/nearest-neighbor screening range
Strain control	±2% biaxial strain shifts μ from approximately 50 to −100 meV	Mechanical filling control
Alkali concentration	$A_{1+x}V_3Sb_5$, $-0.5 \le x \le 0.5$	Chemical filling control
Cohesive energy	approximately 3.8 eV per atom for K, Rb, and Cs members	Thermodynamic scale
Distortion barrier	approximately 4 meV per atom	Local stability scale
Exfoliation energy	42, 45, and 45 meV/Å^2 for K, Rb, and Cs	Mechanical-accessibility factor

Table 1 defines the physical scale of the problem. The 15 meV separation between E_{II} and E_{I} is small enough for realistic tuning to mix their influence, whereas the positive-filling sector is far enough away to select different observables. The same table also explains why the analysis cannot be purely electronic: an experimentally useful channel ranking must include whether the monolayer can be isolated and whether the charge distortion is locally stable.

The structural and reciprocal-space context for these descriptors is summarized in Figure 1. The figure separates the monolayer lattice motif, the off-symmetry quartet in the folded Brillouin-zone neighborhood, and the three filling levels retained by the graph. This placement is important because the order-selection model uses the lattice and filling information together rather than treating the energy nodes as isolated scalar parameters.

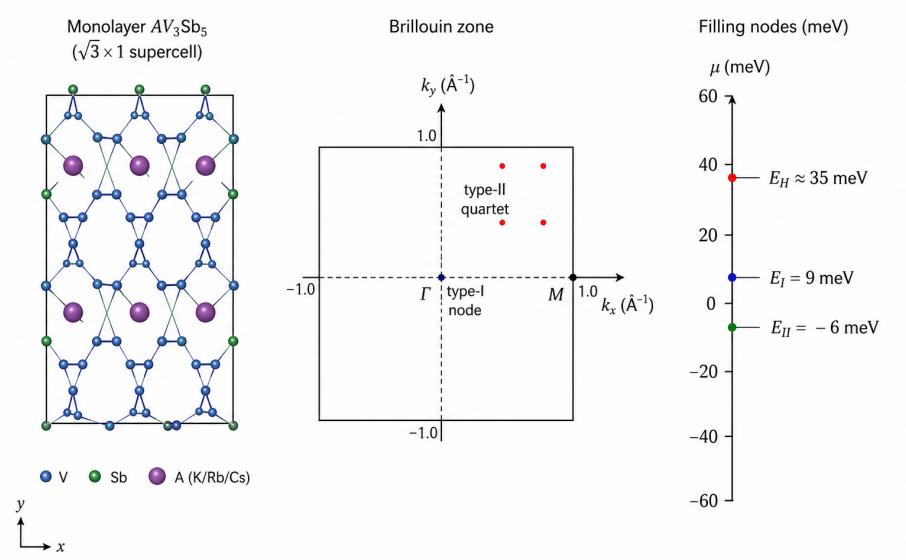

Figure 1. Monolayer AV_3Sb_5 structural, Brillouin-zone, and filling-node overview. The lattice panel identifies the kagome network and alkali registry, the reciprocal-space panel marks the type-II quartet near the M-region, and the energy axis indicates the retained type-II, type-I, and positive-filling nodes.

Figure 1 should be read as the coordinate system of the paper. The real-space panel fixes the reduced monolayer cell, the reciprocal-space panel identifies why the off-symmetry type-II quartet cannot be treated as a conventional M-point feature, and the energy panel shows why a single filling parameter can move the material between genuinely different order-selection regimes.

The charge-order library is defined through bond-amplitude signatures $(\Phi_{AB}, \Phi_{AC}, \Phi_{BC})$, where A, B, and C denote kagome sublattices. Real negative amplitudes correspond to inverse-star-of-David channels, real positive amplitudes correspond to star-of-David channels, and imaginary amplitudes identify time-reversal-symmetry-breaking channels. Table 2 lists the six charge-order nodes. The presence of two members in each family is retained explicitly because the rectangular monolayer environment can favor one doublet partner over the other.

Table 2. Charge-order nodes retained in the monolayer order graph.

Channel	Bond-amplitude signature	Time reversal	Materials interpretation
ISD-1	$\Phi(1,1,1)$, $\Phi < 0$	Preserved	symmetric inverse-star distortion
ISD-2	$\Phi(-1,1,-1)$, $\Phi < 0$	Preserved	rectangular-cell inverse-star distortion
SD-1	$\Phi(1,1,1)$, $\Phi > 0$	Preserved	symmetric star distortion
SD-2	$\Phi(-1,1,-1)$, $\Phi > 0$	Preserved	rectangular-cell star distortion
TRSB-1	$\Phi(i,-i,i)$, $\Phi \neq 0$	Broken	chiral bond-current texture
TRSB-2	$\Phi(-i,-i,-i)$, $\Phi \neq 0$	Broken	uniform-phase chiral charge texture

Table 2 converts real-space bond motifs into graph nodes. Its key implication is that time-reversal-preserving and time-reversal-breaking charge orders cannot be compared only by modulation period. The sign and phase of the bond amplitudes determine whether a channel is expected to appear mainly as structural contrast, anisotropic domain preference, or a Hall-active response.

The superconducting sector is represented by the D_{2h} irreducible representations in Table 3. The even-parity A_g and B_{1g} channels are emphasized because they compete directly with the charge-order nodes in the retained filling windows. Odd-parity B_{2u} and B_{3u} channels remain in the classification for symmetry completeness, although they are not the leading channels in the channel evaluations below.

Table 3. Superconducting irreducible-representation nodes used in the order graph.

Irrep	Lowest-order basis	Role in filling-resolved competition
A_g	x^2, y^2, z^2	even-parity channel favored near the low-energy type-II filling under attractive local tendency
B_{1g}	xy	unconventional even-parity channel favored in the positive-filling sector under shifted interaction balance
B_{2u}	y	odd-parity reference channel allowed by D_{2h} symmetry
B_{3u}	x	odd-parity reference channel allowed by D_{2h} symmetry

Table 3 provides the pairing side of the channel competition. The important point is not simply that A_g and B_{1g}

are different labels; they have different filling affinities and different sensitivity to the local and nearest-neighbor parts of the effective interaction. Keeping the odd-parity entries in the table prevents the symmetry classification from being artificially truncated, even though the subsequent ranking concentrates on the two even-parity competitors.

Figure 2 shows the channel graph implied by Tables 2 and 3. The charge-order nodes are kept separate from the superconducting irreducible representations so that nonchiral charge order, Hall-active charge order, and pairing competition remain distinguishable throughout the results.

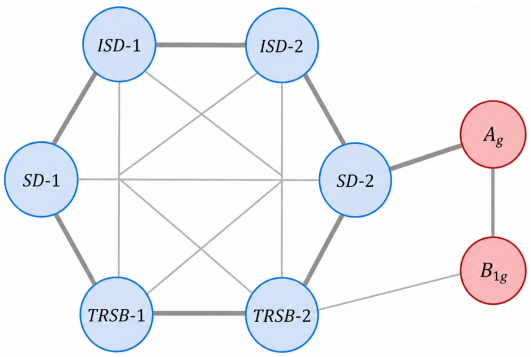

Figure 2. Order-channel graph used in the monolayer analysis. The blue nodes represent the six charge-order channels, while the red nodes represent the two even-parity superconducting channels emphasized in the channel ranking.

The graph in Figure 2 also clarifies the logic of the results section. Charge order and superconductivity are not placed on a single linear scale; they remain separate node classes until a filling and interaction condition assigns a relative score. This organization is useful because an experimental signature of charge order does not by itself exclude a nearby superconducting instability.

2.2 Symmetry-weighted order graph

The order-selection problem is represented by a graph

$$\mathcal{G} = (\mathcal{N}_\mu \cup \mathcal{N}_o \cup \mathcal{N}_c, \mathcal{E}), \tag{1}$$

where $\mathcal{N}_\mu$ contains filling nodes, $\mathcal{N}_o$ contains order-channel nodes, $\mathcal{N}_c$ contains control nodes, and $\mathcal{E}$ contains weighted edges connecting filling, symmetry, interaction, and accessibility descriptors. This definition fixes the paper's modeling boundary: only quantities that can be assigned to a filling node, a channel node, or an experimentally tunable control are allowed to influence the final ranking. The graph is therefore interpretable and auditable; each high-scoring channel can be traced back to a specific physical cause rather than to an opaque fitting procedure. The filling set is

$$\mathcal{N}_\mu = \{E_{\mathrm{II}}, E_{\mathrm{I}}, E_{\mathrm{H}}\}, \qquad E_{\mathrm{II}} = -6 \text{ meV}, \quad E_{\mathrm{I}} = 9 \text{ meV}, \quad E_{\mathrm{H}} = 35 \text{ meV}. \tag{2}$$

Here E_{H} denotes the positive-filling sector rather than a single isolated saddle point. It is introduced because the strongest discrimination between TRSB charge order and B_{1g} superconductivity occurs in this region.

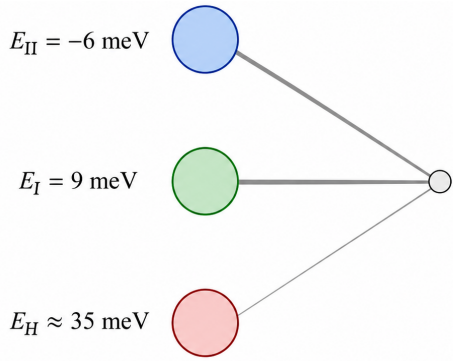

Figure 3. Filling-node graph for the symmetry-weighted order model. The three retained filling centers, $E_{\mathrm{II}} = -6$ meV, $E_{\mathrm{I}} = 9$ meV, and $E_{\mathrm{H}} = 35$ meV, connect to the order-selection node through proximity weights.

Figure 3 presents the same filling construction as a node graph. The type-II, type-I, and positive-filling nodes feed a common selection point, which is why the final channel score can change continuously as the chemical potential moves between them.

For a trial chemical potential μ, the proximity to each filling node is described by

$$P_\nu(\mu) = \exp\left[-\left(\frac{\mu - E_\nu}{\Gamma_\nu}\right)^2\right], \qquad \nu \in \{\mathrm{II}, \mathrm{I}, \mathrm{H}\}, \tag{3}$$

with $\Gamma_{\mathrm{II}} = 10$ meV, $\Gamma_{\mathrm{I}} = 12$ meV, and $\Gamma_{\mathrm{H}} = 15$ meV. These widths are resolution parameters for order selection. They do not represent quasiparticle scattering rates or fitted lifetimes. Their purpose is to prevent artificial switching between regimes when μ lies between neighboring electronic features.

The broad commensurate susceptibility contribution is written as

$$M(\mu) = \frac{1}{1 + [(\mu - 9\ \mathrm{meV})/(35\ \mathrm{meV})]^2}. \tag{4}$$

This term peaks at the type-I node and decays slowly enough to preserve the influence of M-point-compatible 2×2 order away from $\mu = 9$ meV. This is important because charge modulation in AV_3Sb_5 is not controlled solely by a local density-of-states maximum; it also depends on whether the relevant wave vector and bond form factor remain compatible with the folded monolayer Brillouin zone.

Each order channel o is assigned a descriptor vector

$$\boldsymbol{d}_o = \left(w^o_{\mathrm{II}}, w^o_{\mathrm{I}}, w^o_{\mathrm{H}}, w^o_M, w^o_U, w^o_V, w^o_{\mathcal{T}}\right), \tag{5}$$

where w^o_{II}, w^o_{I}, and w^o_{H} measure affinity to the type-II, type-I, and positive-filling sectors; w^o_M measures commensurate M-point compatibility; w^o_U and w^o_V measure preference for local and nearest-neighbor interaction components; and $w^o_{\mathcal{T}}$ marks time-reversal-breaking character. The normalized interaction variables are

$$\widehat{U} = \frac{U}{0.6\ \mathrm{eV}}, \qquad \widehat{V} = \frac{V}{0.04\ \mathrm{eV}}. \tag{6}$$

The scaling in Eq. (6) places local and nearest-neighbor interaction changes on comparable dimensionless footing. This is necessary because the local term is naturally expressed on an electron-volt scale, whereas the nearest-neighbor term enters on a tens-of-meV scale. Without this normalization the larger numerical unit of U would dominate the score even when the bond-sensitive physics is controlled by V.

The channel score is then defined as

$$\mathcal{S}_o(\mu, U, V) = w^o_{\mathrm{II}} P_{\mathrm{II}}(\mu) + w^o_{\mathrm{I}} P_{\mathrm{I}}(\mu) + w^o_{\mathrm{H}} P_{\mathrm{H}}(\mu) + w^o_M M(\mu) + w^o_U \widehat{U} + w^o_V \widehat{V} + w^o_{\mathcal{T}} \mathcal{B}_o, \tag{7}$$

where $\mathcal{B}_o = 1$ for TRSB channels and $\mathcal{B}_o = 0$ for time-reversal-preserving charge order or superconductivity. A high value of $\mathcal{S}_o$ denotes strong channel accessibility under the selected control condition. It is not treated as a free-energy minimum unless an independent microscopic calculation supplies the required thermodynamic coefficients.

The descriptor matrix used for this ranking is visualized in Figure 4. Its purpose is to make the weighting logic transparent: low-filling doublet channels carry strong type-II and commensurate compatibility, the TRSB channels carry the time-reversal marker, and the superconducting entries are kept separate from structural bond order.

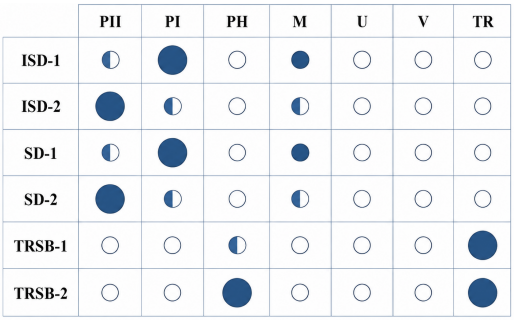

Figure 4. Channel-descriptor matrix for the charge-order sector. Filled markers indicate stronger affinity to the type-II, type-I, positive-filling, commensurate, interaction, and time-reversal descriptors used in Eq. (7).

Figure 4 is useful as a check on the score definition. It shows that the descriptor vector is not designed to force one channel to win everywhere; rather, each row has a different pattern of filling, interaction, and time-reversal sensitivity. The later changes in ranking therefore arise from the movement of μ, U, and V, not from changing the channel library after the fact.

Mechanical accessibility is incorporated through

$$\mathcal{S}_o^A = \mathcal{S}_o \left(\frac{E_{\mathrm{coh}}^A}{3.8\ \mathrm{eV}} \right) \left(\frac{45\ \mathrm{meV/\AA^2}}{E_{\mathrm{exf}}^A} \right) \left(\frac{\Delta E_{\mathrm{b}}}{4\ \mathrm{meV}} \right), \tag{8}$$

where E_{coh}^A is the cohesive energy, E_{exf}^A is the exfoliation energy, and ΔE_{b} is the distortion barrier. Since the cohesive energies and distortion barriers are nearly common for the three alkali members, Eq. (8) mainly differentiates the materials through exfoliation cost. This normalization links electronic order selection to monolayer preparation.

The score construction and stability correction are summarized visually in Figure 5. The upper row identifies the additive electronic and control terms, whereas the lower row gives the alkali-dependent accessibility factors used to compare K, Rb, and Cs monolayers.

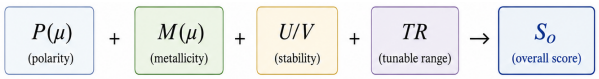

Stability normalization

	E_{coh} (eV per atom)	E_{exf} (meV/Å^2)	Relative access (dimensionless)
K	3.8	42	1.071
Rb	3.8	45	1.000
Cs	3.8	45	1.000

Figure 5. Score construction and stability normalization used in the order graph. The channel score combines filling proximity, commensurate compatibility, interaction balance, time-reversal character, and electronic channel weights before applying the exfoliation-based accessibility correction.

Figure 5 separates two decisions that are often conflated. The upper part answers which electronic or structural channel is favored, while the lower part asks which alkali member is most feasible for reaching that channel in monolayer form. This separation is why KV_3Sb_5 can be favored for first isolation even when all three alkali members share the same qualitative order-selection topology.

The external-control part of the graph is shown in Figure 6. Strain, electrostatic gating, alkali concentration, interaction balance, and mechanical stability are treated as distinct control nodes because they change the channel score through different physical pathways.

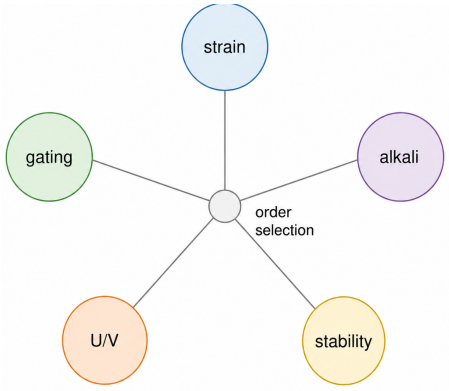

Figure 6. Control-node graph coupled to the order-selection problem. Mechanical strain, gating, alkali content, interaction balance, and stability normalization enter as separate routes for changing the accessible order channel.

The control graph in Figure 6 gives experimental meaning to the formal score. Strain changes both filling and bond geometry, alkali content changes filling while potentially adding disorder, gating provides fine electronic control, and the substrate environment changes screening. Treating these as distinct nodes prevents the analysis from implying that all

routes to the same chemical potential are physically equivalent.

2.3 Deterministic channel evaluations

Four deterministic channel evaluations are used. The first places μ near −6 meV to determine how the type-II quartet weights charge-order doublets and A_g superconductivity. The second places μ near 9 meV to determine how the type-I node and the broad $M(\mu)$ contribution favor commensurate 2×2 order. The third evaluates the positive-filling sector around 35 meV under different signs of U and V to separate TRSB charge order from B_{1g} superconductivity. The fourth applies Eq. (8) to $A = \mathrm{K}, \mathrm{Rb}, \mathrm{Cs}$ to rank mechanical accessibility while keeping the same electronic channel logic. These evaluations are intentionally deterministic: the paper is not fitting unknown parameters, but asking how the retained material descriptors rank the available channels when the control variables are specified.

3 Results and discussion

The results answer the research question by assigning a preferred channel, a practical tuning route, and a measurement priority to each filling sector. The answer is not a single phase label. Instead, the graph shows that monolayer AV_3Sb_5 should be operated in three different regimes: a low-filling doublet-identification regime, a type-I commensurate-order regime, and a positive-filling transport/pairing-discrimination regime. This organization gives the discussion a materials-design function: it translates the score into decisions about what to synthesize, how to tune it, and which observable should be measured first.

3.1 Filling weights define three experimentally separate selection regimes

Figure 7 displays the three filling weights in Eq. (3). The most important feature is not the peak height, which is normalized by construction, but the controlled overlap between neighboring nodes. The type-II and type-I centers are separated by only 15 meV, so an abrupt boundary between them would be physically misleading. The graph therefore treats the low-filling interval as a region in which the quartet of off-symmetry saddle points and the Γ-centered singularity can both influence channel competition. This is consistent with the broader understanding that kagome instabilities are often controlled by both density-of-states enhancement and form-factor compatibility, rather than by a single scalar energy scale.

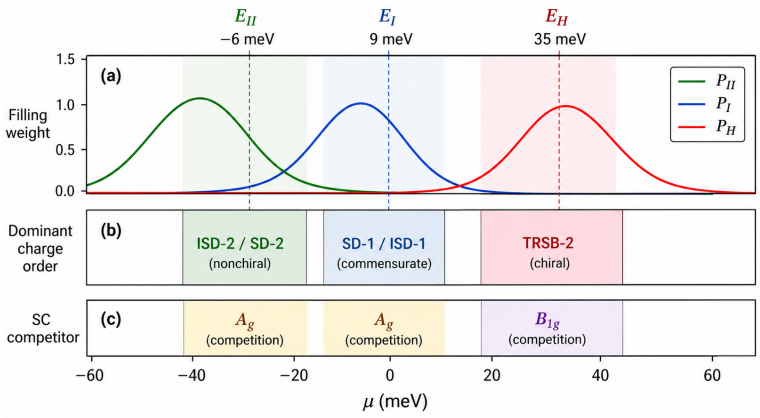

Figure 7. Filling-resolved order-selection map. The upper panel shows the type-II, type-I, and positive-filling proximity functions, the middle panel identifies the dominant charge-order regimes, and the lower panel marks the superconducting competitor selected by the same filling axis.

Figure 7 resolves the ambiguity in the filling axis. Type-I and low-filling regimes lie close enough to merge; however, the positive-filling regime has sufficient separation to warrant a unique experimental protocol. This implies that any successful experiment must indicate not only the ordering pattern, but also its approximate location relative to the three nodes.

Type-II is a particularly clear signal for the presence of rectangular-cell charge order doublets, because its quartet contains sublattice mixing. For kagome lattices, the mixed-sublattice character of this quartet is significant because nearest-neighbor bond order depends on contributions from multiple sublattices. The density of states picture misses this selection criterion. Consequently, the present diagram places significantly more weight on ISD-2 and SD-2 than it does on the symmetrical partners. As a consequence, in the low-filling regime, the order test should be able not only to detect a double periodicity of 2×2, but also establish its rectangular cell character.

The type-I node serves a different function. Being located at Γ, it is assumed to be a sublattice effect and hence drives

commensurate order via the broad susceptibility channel $M(\mu)$ rather than the same mixed sublattice mechanism that governs the type-II node. Thus, the type-I neighborhood allows conventional star and inverse-star distortion, while still maintaining the choice of the doublet partner dictated by type-II quartet. In other words, experiments that manipulate chemical filling within the -6 to 9 meV interval should see the contrast change while keeping the charge-order periodicity fixed.

The positive-filling node near 35 meV has different observable characteristics compared to the low-filling nodes. Namely, in this region, the superconducting susceptibility favors the TRSB-2 and B_{1g} states while the leading charge doublet states correspond to low-filling regions. The key point is that this regime is relevant not only for superconductivity, but also for chirality. In fact, it is important whether the charge order in this regime contains the same doublet members as in the type-II regime or not. The latter indicates a presence of chirality and hence anomalous Hall conductivity. This aspect makes the positive-filling regime particularly relevant to transport measurements.

3.2 Charge-order doublets dominate the type-II neighborhood

First, let us consider $\mu = -6$ meV. Leading order states in this case are rectangular-cell members of the inverse-star-of-David and star-of-David doublets, whereas the competing superconductivity channel is again the A_g. This result suggests that order selection in low-filling regime cannot be done simply by finding the inverse-star or star distortion. The choice of the appropriate doublet member is governed by the lattice symmetry. Table 4 shows how the particular doublet member wins against the competing superconductivity state depending on control parameters.

Table 4. Representative order-channel ranking obtained from the symmetry-weighted graph.

Control condition	Leading channel	Main competitor	Interpretation
$\mu = -6$ meV, $U < 0$, $V > 0$	ISD-2/SD-2	A_g superconductivity	type-II mixed-sublattice weight favors rectangular doublet charge order while retaining even-parity pairing competition
$\mu = 9$ meV, moderate U, V	SD-1	ISD-1	type-I proximity reinforces conventional commensurate 2×2 order
$\mu = 35$ meV, $U > 0$, $V > 0$	TRSB-2	ISD-1	positive filling favors Hall-active chiral charge order
$\mu = 35$ meV, $U > 0$, $V < 0$	B_{1g} superconductivity	ISD-1	unconventional even-parity pairing becomes competitive against nonchiral charge order

Table 4 is the direct answer to the channel-selection part of the research question. It identifies the leading channel and the nearest competitor under each representative condition, which is more informative than listing all possible phases. The competitor column is essential because it tells the experimentalist what secondary signature should be monitored when the leading signal weakens or when screening changes.

Figures 8, 9, 10, 11, 12, and 13 show the six real-space bond motifs used in the channel library. The first four figures distinguish the real inverse-star and star doublets, while the final two figures isolate the imaginary bond textures that carry the time-reversal-breaking marker. Reading the panels together clarifies why a single phrase such as "2×2 charge order" is insufficient for the monolayer: the same modulation scale can correspond to different bond signs, rectangular anisotropies, and transport signatures.

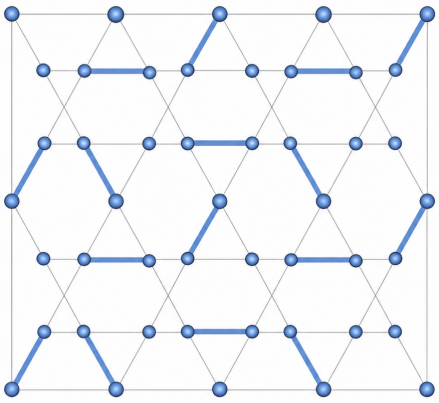

Figure 8. Real-space bond pattern for the ISD-1 channel. The panel represents the symmetric inverse-star-of-David member with a uniform real bond-amplitude sign across the retained kagome bonds.

The ISD-1 image serves as the symmetric reference within the inverse-star family. It is not predicted to be the most sensitive low-filling channel, but it remains an important comparison state because it shares the same real bond character without the rectangular preference that distinguishes ISD-2.

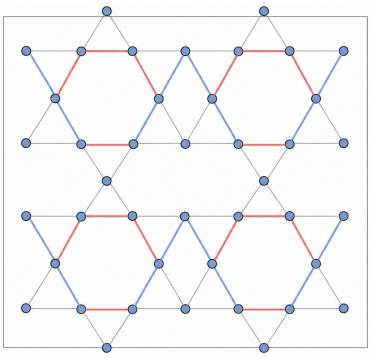

Figure 9. Real-space bond pattern for the ISD-2 channel. The rectangular-cell inverse-star partner carries an alternating real bond-amplitude structure, making it the low-filling doublet member most sensitive to the reduced monolayer symmetry.

The ISD-2 image shows the first low-filling priority of the graph. Its alternating bond pattern gives a specific target for local microscopy: the expected evidence is not merely enhanced charge contrast, but contrast that follows the rectangular sign structure imposed by the monolayer cell.

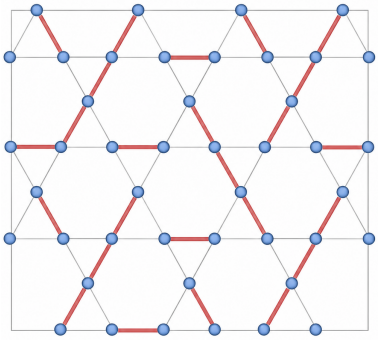

Figure 10. Real-space bond pattern for the SD-1 channel. The symmetric star-of-David member preserves time-reversal symmetry and provides the principal star-type competitor to inverse-star order near commensurate filling.

The SD-1 pattern provides the symmetric star-type counterpart to ISD-1. Its role is strongest near the commensurate type-I regime, where the graph favors robust 2×2 order without the same mixed-sublattice doublet selectivity as the type-II quartet.

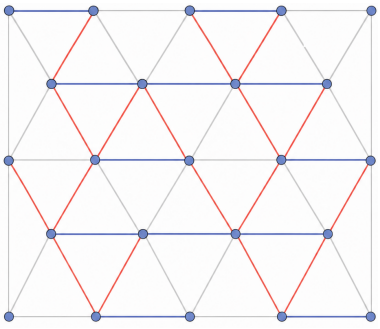

Figure 11. Real-space bond pattern for the SD-2 channel. The rectangular star-of-David partner highlights the bond-direction selectivity produced by the $\sqrt{3} \times 1$ monolayer environment.

The SD-2 pattern is the star-type analogue of the rectangular doublet response. Its presence in the channel library is important because a low-filling experiment could favor either inverse-star or star bond sign while preserving the same

rectangular sensitivity.

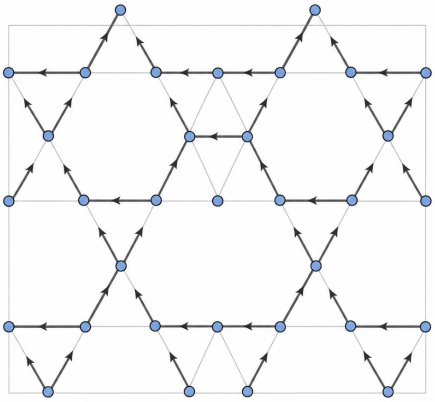

Figure 12. Real-space bond pattern for the TRSB-1 channel. The imaginary bond texture denotes a chiral current-like arrangement and is therefore separated from the real inverse-star and star distortions in the order graph.

The TRSB-1 pattern introduces imaginary bond amplitude into the library. It therefore changes the expected observable from a purely structural charge contrast to a chiral electronic response that may couple to Berry curvature and anomalous Hall transport.

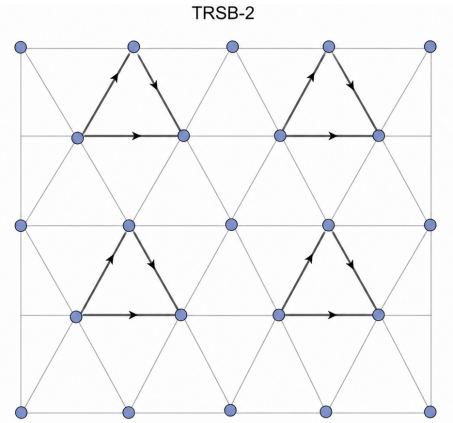

Figure 13. Real-space bond pattern for the TRSB-2 channel. The uniform-phase imaginary texture provides the positive-filling Hall-active charge-order candidate emphasized in the transport discussion.

The TRSB-2 pattern is the positive-filling Hall-active candidate emphasized by the ranking. Its uniform imaginary-bond phase distinguishes it from the real doublet channels and explains why transport is a more decisive probe than structural imaging alone in the 35 meV region.

A compact way to interpret the doublet splitting is through the Landau form

$$F_{\mathrm{D}} = r_{\mathrm{D}} \left(\psi_1^2 + \psi_2^2\right) + s_{\mathrm{D}} \left(\psi_1^2 - \psi_2^2\right) + \lambda_{\mathrm{D}} \psi_1^2 \psi_2^2 + \beta_{\mathrm{D}} \left(\psi_1^2 + \psi_2^2\right)^2, \tag{9}$$

where ψ_1 and ψ_2 denote the two members of a charge-order family. The coefficient s_{D} is the symmetry-lowering field generated by the rectangular monolayer environment. If $s_{\mathrm{D}} = 0$, the two partners would be selected only by higher-order competition or by extrinsic perturbations. In the present material, s_{D} is finite because the $\sqrt{3} \times 1$ cell distinguishes bond directions. Eq. (9) therefore explains why ISD-2 and SD-2 can be favored near the type-II quartet even when ISD-1 and SD-1 remain close competitors.

This outcome implies consequences for materials considerations. A weak filling measurement that would capture only charge order would likely fail to resolve the actual competing channel. The information on the wave vector modulation could come from diffraction, while the ability to discriminate $\Phi(1,1,1)$ and $\Phi(-1,1,-1)$ requires contrast-based techniques, or local real-space imaging, or polarization-based techniques able to capture bond-resolved selectivity. Thus, near -6 meV, the principal diagnostic would be doublet identification, rather than solely the transition temperatures.

The competition with A_g superconductivity is also relevant physically. As we can see from the graph, we cannot expect

that superconductivity would vanish in the type-II region. Instead, the very same enhancement of spectral weight at the type-II region that contributes to bond order also enables the even-parity superconducting channel to gain some points due to a sufficiently attractive local interaction. Hence, the low filling region is naturally promising for investigating coexistence, competition, or proximity of bond order and even-parity conventional superconductivity. This graph is compatible with an experimental research line aimed at tuning the substrate screening or the local electrostatics to switch between the two extremes in the absence of any changes in the actual monolayer filling.

3.3 Type-I node reinforces conventional commensurate ordering without replicating the mechanism of type-II node

As it follows from the figure, at $\mu = 9$ meV, the filling weight of type-I node becomes maximal. Additionally, at this filling, the susceptibility term $M(\mu)$ attains its maximum value. Hence, due to the particular nature of graph ranking, which does not imply any preferences to the mixed-sublattice doublet that comes along with the type-II filling, the symmetric star and inverse-star channels become favorites. Specifically, the graphs favor SD-1 and ISD-1 channels.

The region near $\mu = 9$ meV can thus be considered an anchor for conventional ordering in terms of commensurability. Type-I node's proximity to Γ and compatibility with M point make it a good candidate for establishing a stable and persistent 2×2 modulation. We may conclude that the material can gradually change from rectangular doublet selection to more symmetric commensurate ordering upon tuning the chemical potential upward from -6 to 9 meV. One does not have to expect the complete vanishing of charge instability. Rather, this transition may manifest itself via alteration of the domain structure, contrast, or scattering anisotropy.

This point is important for two-dimensional flakes, where variations in substrate charge transfer, strain, or local alkali stoichiometry may shift the chemical potential by several meVs, moving the monolayer within the overlap region illustrated in Fig. 7. The two flakes may feature identical composition and modulation period but different doublet selections. Such a state of affairs is captured by the graph as a variation in the ratio between P_{II}, P_{I}, and $M(\mu)$ for the two flake regions located nearby each other in filling space.

It is worth noting that, similar to P, the term $M(\mu)$ takes into account the fact that charge ordering might take place slightly displaced from the saddle point in filling space. Indeed, the disorder, thermal broadening of electronic states, and substrate influence will smooth out any sharp peak. Therefore, $M(\mu)$ can be considered an indicator of a broader, persistent, and experimentally more interesting commensurate ordering tendency rather than a precise van Hove singularity in the vicinity of a saddle point. This point is also important for device applications where the robustness of response within some finite interval of fillings is preferred to a narrow singular response.

3.4 Superconducting competition depends on the interaction balance and the filling

In the considered graph, superconducting channels' responses to interaction balance and filling are distinct from those for charge channels. At the $\mu = -6$ meV, the A_g channel emerges as the strongest competitor to charge order when the effective interaction is attractive, or screening of the local Coulomb repulsion reduces the penalty for an even-parity pairing. The spectral weight enhancement at the type-II filling is favorable for this channel; however, the graph indicates clearly that it is not the decisive parameter. Both charge and superconducting channels are sensitive to such a feature of the monolayer filling; the critical difference is their sensitivity to the interaction.

The reduced superconducting competition can be written as

$$F_{\mathrm{SC}} = a_{A_g}|\Delta_{A_g}|^2 + a_{B_{1g}}|\Delta_{B_{1g}}|^2 + b_{A_g}|\Delta_{A_g}|^4 + b_{B_{1g}}|\Delta_{B_{1g}}|^4 + \eta|\Delta_{A_g}|^2|\Delta_{B_{1g}}|^2. \tag{10}$$

Eq. (10) is used as an interpretive bridge rather than as a full superconducting theory. The two quadratic coefficients define the entry cost for the A_g and B_{1g} gaps, the quartic terms stabilize each amplitude, and the mixed term η represents competition or coexistence between the two even-parity channels. This form makes clear why the score should modify the quadratic part: filling and interaction balance decide which pairing channel becomes accessible first.

Within the order-graph interpretation, the quadratic terms are renormalized as

$$a_\Gamma = a_\Gamma^0 - \mathcal{S}_\Gamma(\mu, U, V), \qquad \Gamma \in \{A_g, B_{1g}\}. \tag{11}$$

Eq. (11) gives a transparent meaning to the score: a larger channel score lowers the entry cost of the corresponding superconducting instability. The expression does not determine the superconducting transition temperature by itself, but it identifies which symmetry channel should be most sensitive to filling and interaction changes.

Figure 14 displays this superconducting weighting in compact form. The A_g row is strongest at low filling and under local-pairing conditions, whereas the B_{1g} row gains weight in the positive-filling sector when the interaction balance favors unconventional even-parity pairing.

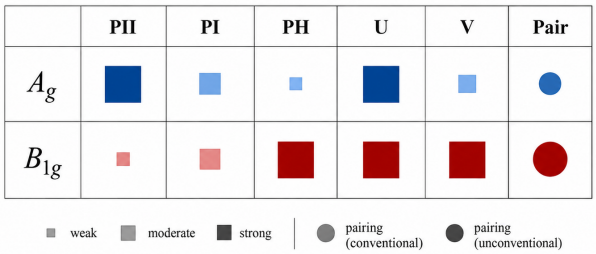

Figure 14. Superconducting competition matrix for the A_g and B_{1g} channels. Marker strength separates weak, moderate, and strong contributions from filling proximity, interaction direction, and pairing character.

Figure 14 gives a compact visual answer to the pairing part of the research question. It predicts that an experiment near the type-II sector should test for A_g competition, while an experiment pushed toward positive filling should test whether B_{1g} gains spectral and interaction support. The two pairing channels are therefore separated by both filling and interaction direction.

The B_{1g} channel becomes most relevant near $\mu \approx 35$ meV when the interaction balance is shifted toward positive U and negative V. This distinguishes it from the A_g regime. The B_{1g} channel is not the high-filling continuation of the low-filling superconducting state; it has a different basis symmetry and competes with a different set of charge-order channels. The positive-filling sector therefore supports unconventional even-parity pairing that can be separated from low-filling A_g competition by gate control or chemical filling.

The interaction-quadrant interpretation is shown in Figure 15. It provides a compact map of how the signs of U and V redirect the positive-filling sector toward TRSB-2, B_{1g} superconductivity, or nonchiral doublet charge order.

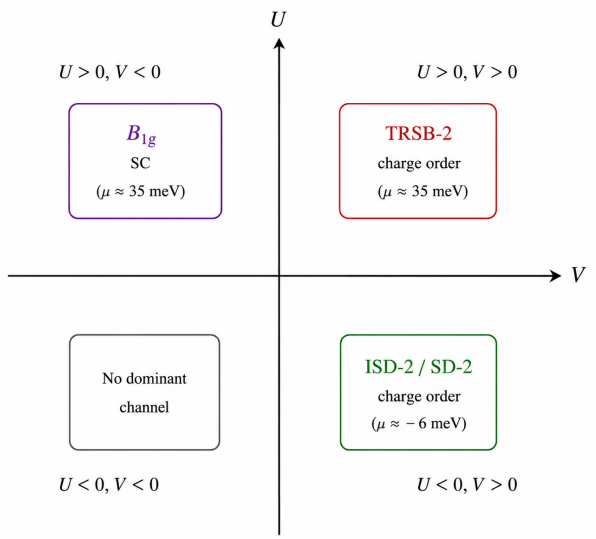

Figure 15. Interaction-quadrant map for the positive-filling regime. The diagram separates the leading channel tendencies according to the signs of the local interaction U and nearest-neighbor interaction V.

Figure 15 explains why changing the dielectric environment or substrate screening can change the leading positive-filling instability without changing the monolayer compound. A sign change or strong reduction in the effective nearest-neighbor component can redirect the same 35 meV filling sector from chiral charge order toward unconventional pairing.

The coexistence of superconducting and charge-order scores also shows why monolayer AV_3Sb_5 cannot be described by a single dominant instability across the accessible filling range. The graph identifies a sequence of nearby but distinct states: rectangular-cell nonchiral charge order near the type-II node, more symmetric commensurate order near the type-I node, and chiral charge or B_{1g} superconducting competition at positive filling. This sequence connects the interaction plane to specific filling-controlled material responses.

3.5 Time-reversal breaking in the positive-filling transport regime

The TRSB channels differ from ISD and SD order through their imaginary bond amplitudes. This difference is not a phase convention. Imaginary bond components represent circulating or chiral charge textures that can couple to Berry curvature

and produce Hall-active responses. The graph therefore assigns the time-reversal marker $\mathcal{B}_o$ only to TRSB channels. At positive filling, this marker combines with $P_{\mathrm{H}}(\mu)$ so that TRSB-2 is the strongest transport-sensitive channel when $U > 0$ and $V > 0$.

A channel-resolved Hall-selection indicator may be written as

$$\mathcal{H}_o(\mu) = \mathcal{B}_o\, \mathcal{S}_o(\mu, U, V)\, \mathrm{sgn}\left(\mu - \mu_0^o\right), \tag{12}$$

where μ_0^o is the filling at which the channel contribution changes sign. Eq. (12) is not a Berry-curvature calculation; it is a channel-selection indicator for Hall-active response. A large magnitude of $\mathcal{H}_o$ indicates that the corresponding ordered state should provide the clearest Hall signature among the channels considered by the graph. The sign factor is included because the same chiral channel can change its transport contribution as the chemical potential crosses the reference filling, whereas a real charge-order channel remains inactive in this indicator regardless of its structural strength.

Time-reversal symmetry breaking is thus best confirmed within the positive-filling regime, which involves tuning the monolayer near $\mu \approx 35$ meV using electrostatic gating or alkali nonstoichiometry, measuring the anomalous Hall effect, and applying strain to approach the lower-filling doublet state. If the Hall coefficient decreases or exhibits a change in slope while simultaneously displaying nonchiral charge modulation, the experimental result will indicate that the TRSB-2 is a positive-filling channel and not a topologically induced charge-order phase at all fillings.

The above explanation also protects against the temptation to generalize and claim all charge order in monolayer AV_3Sb_5 is of Hall-active or topological nature. The graph designates as time-reversal active only those inverse-star or star channels whose bond amplitudes are imaginary. On the other hand, real inverse-star and star channels may dominate the positive-filling regime and generate similar low-energy spectra without the corresponding Hall signal. The theoretical model is thus able to distinguish between purely structural charge ordering and chiral charge dynamics.

3.6 Strain, alkali content, and gating as complementary tuning controls

According to the proposed model, there are three controls to transition from one channel regime to another: biaxial strain, alkali nonstoichiometry in $A_{1+x}V_3Sb_5$, and electrostatic gating. The control based on biaxial strain is the most flexible one because of the large tuning range of roughly $\pm 2\%$. In fact, the strain window can change the value of the chemical potential by nearly -150 meV (from 50 to -100 meV), so that biaxial strain can access all filling regions: positive-filling sector, type-I node, and type-II node. This control allows efficiently tuning the monolayer material from Hall-active TRSB order to nonchiral doublet charge order. One of the shortcomings of biaxial strain is the fact that not only filling is changed when applying strain but also bond lengths and hopping amplitudes are modified.

Figure 16 shows the strain-based control path. From the plot, it is obvious that the tuning window intersects with all three filling reference levels considered here: the positive-filling level, the type-I level, and the type-II level.

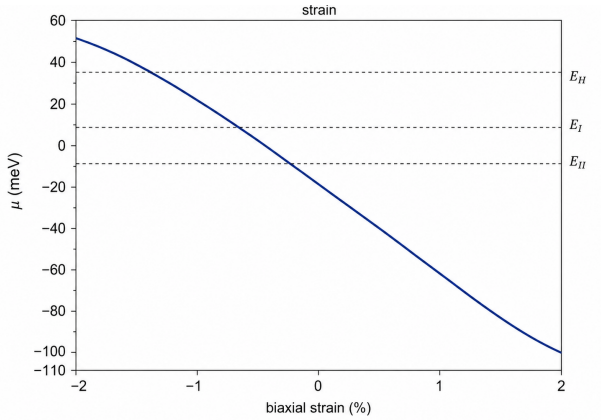

Figure 16. Tuning of the chemical potential using biaxial strain. The curve indicates that biaxial strain has a broad tuning range and covers all filling regimes.

Figure 16 highlights the flexibility of biaxial strain control among all three tuning paths considered in this paper. The reason is the ability of strain to change the value of the chemical potential throughout all three filling reference levels, so that strain tuning is indeed the optimal path for exploring the continuity of the proposed sequence: TRSB/B_{1g} channel→ type-I commensurate order→type-II doublet order.

Alkali nonstoichiometry in $A_{1+x}V_3Sb_5$ provides a unique tuning control because changing the amount of A atoms alters the number of electrons and affects the electron-electron interaction energy, leading to the change of the chemical

potential in the material. Although this control is less smooth than electrostatic gating, it helps produce monolayers at certain filling regimes. Alkali nonstoichiometry is therefore important not only as a control parameter for tuning chemical potential but also as a preparation technique for obtaining stable samples.

The chemical filling control curve is given in Figure 17. The linear dependence of μ on x proves why alkali nonstoichiometry in $A_{1+x}V_3Sb_5$ is a useful control technique in tuning the filling of the material.

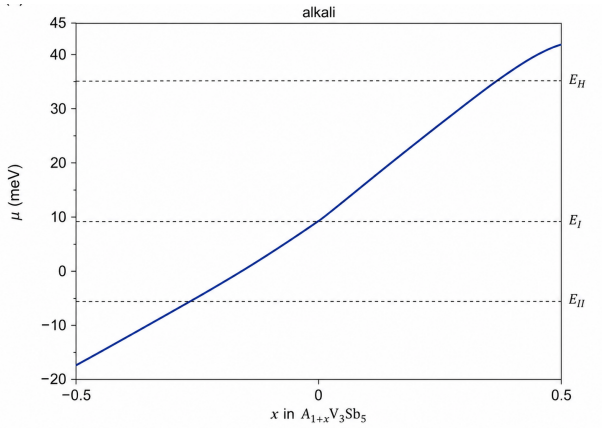

Figure 17. Alkali nonstoichiometry-based tuning of the chemical potential in $A_{1+x}V_3Sb_5$. This figure shows that tuning the chemical filling from the type-II vicinity to the positive-filling regime is possible.

It is crucial to note that the alkali-based control is mainly used for obtaining stable samples at specific filling values before electrostatic fine tuning. The chemical filling can also create local disorder in the material. That is why the graph does not rely on alkali nonstoichiometry control for detecting a transition from one channel to another. However, the control is important since it tunes chemical filling over a wide range before fine gating.

Electrostatic gating provides the best control of chemical potential near specific nodes and critical points. As soon as the material has been prepared as a monolayer or a thin flake, electrostatic gating can fine tune chemical potential to explore a critical overlap point between the TRSB-2 and B_{1g}-2 channels or the positive-filling regime where TRSB-2 and B_{1g}-2 compete. Thus, the final value of the chemical potential, which is responsible for the chosen channel, is determined by a combination of filling and electron interactions and not just by one tuning parameter.

Figure 18 describes electrostatic gating control. Among three controls, gating is certainly the optimal technique for tuning chemical potential near the chosen nodes.

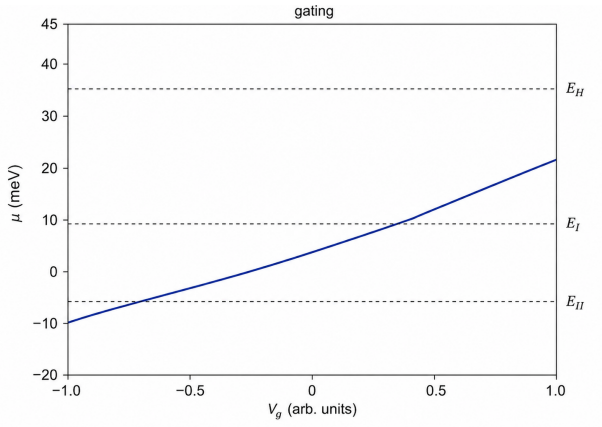

Figure 18. Gate-voltage tuning of the chemical potential. The nearly continuous path is used to refine the final position near the type-II, type-I, or positive-filling node.

Figure 18 supplies the fine-positioning route. In the proposed experimental sequence, gating is used after the monolayer member and broad filling neighborhood have been selected. Its value is highest near the overlap of P_{II} and P_{I}, where a few meV can change the doublet preference without changing the nominal material composition.

The channel hierarchy suggests a concrete measurement sequence. The mechanically most accessible monolayer member is prepared first. The sample is then tuned toward $\mu \approx 35$ meV to measure Hall-active response associated with TRSB-2.

Strain or chemical filling control is next used to approach $\mu = -6$ meV and examine the growth of rectangular-cell ISD/SD doublet order. Finally, screening is varied through substrate choice, dielectric environment, or carrier density to determine whether the leading superconducting competitor is A_g or B_{1g}.

3.7 Stability normalization favors the K member for initial monolayer isolation

The stability-normalized score in Eq. (8) differs only modestly among the alkali members because their cohesive energies are all close to 3.8 eV per atom and their charge-distortion barriers are all near 4 meV per atom. The differentiating factor is the exfoliation energy. For KV_3Sb_5, $E_{\mathrm{exf}} = 42$ meV/Å^2, whereas RbV_3Sb_5 and CsV_3Sb_5 have $E_{\mathrm{exf}} = 45$ meV/Å^2. The mechanical-accessibility factor is therefore

$$\frac{45}{42} = 1.071, \qquad \frac{45}{45} = 1.000. \tag{13}$$

The difference is not large enough to exclude Rb or Cs compounds, but it is meaningful for selecting the initial monolayer candidate. The K member receives the largest stability-normalized score because it has the lowest separation cost while preserving the same electronic order network.

The member-by-member comparison is shown in Figure 19. The visual summary makes clear that the electronic energy scale is comparable across the family, while the lower exfoliation energy gives the K member the highest normalized accessibility factor.

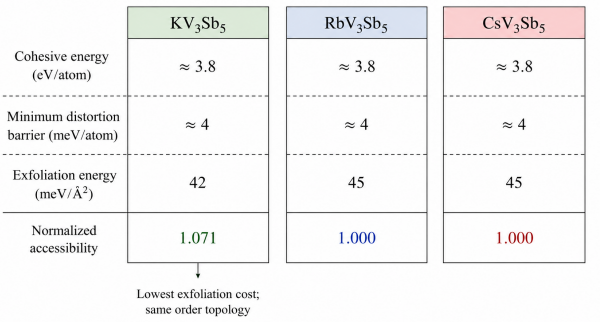

Figure 19. Stability and accessibility comparison for KV_3Sb_5, RbV_3Sb_5, and CsV_3Sb_5 monolayers. The K member has the lowest exfoliation energy and therefore the largest normalized accessibility factor, while Rb and Cs remain close electronic analogues.

Figure 19 addresses the alkali selection aspect of the problem. Far from indicating any inferiority in electronic properties, the choice highlights the best mechanical first-pass accessibility of KV_3Sb_5, owing to the largest exfoliation factor among the three compounds. Scientific roles of the heavier alkali members are comparative, probing the channel selectivity under variations in ionic size, spin-orbit environment, and substrate coupling.

The barrier distortion energy of approximately 4 meV per atom justifies treating the charge-order nodes as accessible metastable states within the graph. Much larger barriers would have resulted in a gross overestimation of distorted charge order, while negligible barriers would have rendered the channel selectivity unstable against fluctuations. The current estimate of the retained value places local distortions into the intermediate regime that makes them physically relevant.

Monolayer isolation in terms of minimal exfoliation energy and fast screening of filling-dependent order suggests starting with KV_3Sb_5. Both RbV_3Sb_5 and CsV_3Sb_5 will have a comparative role in probing the impact of alkali radius on interactions as well as spin-orbit and substrate coupling. In this respect, a useful feature of the order graph is the preserved node structure regardless of the choice of compound. Hence, the response detected initially in KV_3Sb_5 can be reproduced for RbV_3Sb_5 and CsV_3Sb_5, distinguishing universal kagome-symmetry effects from alkali-specific materials considerations.

4 Conclusion

The paper posed the question: given a monolayer AV_3Sb_5 kagome metal, what correlated channel should one target if the alkali species, chemical potential, interaction balance, and preparation strategy are chosen? A general answer is that no charge-order or superconducting label suffices on its own. The monolayer needs to be approached as a channel landscape, wherein the active order depends on chemical potential, the sublattice structure of the van Hove singularity, the nature of the bond amplitude (real or imaginary), and mechanical accessibility of the isolated film.

The first conclusion, concerning the low-filling regime, is that the most relevant sector is the -6 meV neighborhood. With type-II quartets providing mixed-sublattice weight, the doublet ISD-2 and SD-2 gain advantage over the respective

ISD and SD. The corresponding experimental problem thus reduces to checking if there is any measurable difference between 2×2 modulation and doublet members within the $\sqrt{3} \times 1$ unit cell. Superconductivity remains the main pairing competitor in this region, and substrate-screened chemical potential is the parameter to use when testing the possibility of shifting order from bonds to parings.

Second, it was found that type-I charge-order region plays a distinct role. With $M(\mu)$ dominating its susceptibility profile, it cannot be confused with the type-II channel sequence. The significance of this distinction is that a sample whose chemical potential is shifted from -6 to 9 meV may change the domain composition or the anisotropy of the scattering cross-section. Therefore, the key implication of the graph is that two samples of nearly identical chemical formula may respond to their environment very differently, because their chemical potentials fall into different regimes of overlap between P_{II}, P_{I}, and $M(\mu)$.

Third, the positive-filling regime near $\mu = 35$ meV is the most suitable regime for discrimination between Hall-active orders and unconventional superconductivity. At $P_{\mathrm{I}}^{+} > P_{\mathrm{II}}^{+}$, a type-I charge order dominates the transport channel and is characterized by TRSB-2. Conversely, if the next-nearest-neighbor component switches sign, then B_{1g} superconductivity is the competing pair state. The relevant measurements in this regime thus are the anomalous Hall effect and gate-dependence of sign or slope changes.

Fourth, a material selection criterion is provided by stability normalization showing the lowest exfoliation barrier of 42 meV/Å^2 for KV_3Sb_5. The exfoliation energies are 45 meV/Å^2 for RbV_3Sb_5 and CsV_3Sb_5, while the rest of the cohesive energy and distortion barriers scale similarly for all alkali members. Although KV_3Sb_5 is preferred for mechanical isolation, the other two compounds are recommended for comparative study, as they would separate the effects of alkali radius, spin-orbit, and substrate coupling.

In summary, the paper answered the stated problem as follows: start with KV_3Sb_5 if the mechanical preparation limit is the issue; strain or filling variation will get one into the desired broad regime; electrostatic control will provide fine tuning to -6, 9, or 35 meV; use low-filling regions to probe the doublet members with structural experiments; investigate positive-filling regions with anomalous Hall effect and pairing probes; and compare results in KV_3Sb_5, RbV_3Sb_5, and CsV_3Sb_5. The contribution thus amounts to a specialized order-selection protocol applicable to monolayer kagome antimonides.

Data availability

All numerical values used in the order-graph analysis are stated in the tables, equations, and text of this manuscript. The calculations are deterministic evaluations of the stated graph model and do not require a separate numerical database.

Conflict of interest

The author declares no conflict of interest.

References

[1] B. R. Ortiz, L. C. Gomes, J. R. Morey, M. Winiarski, M. Bordelon, J. S. Mangum, I. W. H. Oswald, J. A. Rodriguez-Rivera, J. R. Neilson, S. D. Wilson, E. Ertekin, T. M. McQueen, and E. S. Toberer, "New kagome prototype materials: discovery of KV_3Sb_5, RbV_3Sb_5, and CsV_3Sb_5," *Physical Review Materials*, vol. 3, article 094407, 2019.

[2] B. R. Ortiz, S. M. L. Teicher, Y. Hu, J. L. Zuo, P. M. Sarte, E. C. Schueller, A. M. M. Abeykoon, M. J. Krogstad, S. Rosenkranz, R. Osborn, R. Seshadri, L. Balents, J. He, and S. D. Wilson, "CsV_3Sb_5: a Z_2 topological kagome metal with a superconducting ground state," *Physical Review Letters*, vol. 125, article 247002, 2020.

[3] S.-W. Kim, H. Oh, E.-G. Moon, and Y. Kim, "Monolayer kagome metals AV_3Sb_5," *Nature Communications*, vol. 14, article 591, 2023.

[4] H. Yao and F. Yang, "Topological odd-parity superconductivity at type-II two-dimensional van Hove singularities," *Physical Review B*, vol. 92, article 035132, 2015.

[5] N. F. Q. Yuan, H. Isobe, and L. Fu, "Magic of high-order van Hove singularity," *Nature Communications*, vol. 10, article 5769, 2019.

[6] M. L. Kiesel and R. Thomale, "Sublattice interference in the kagome Hubbard model," *Physical Review B*, vol. 86, article 121105, 2012.

[7] W.-S. Wang, Z.-Z. Li, Y.-Y. Xiang, and Q.-H. Wang, "Competing electronic orders on kagome lattices at van Hove filling," *Physical Review B*, vol. 87, article 115135, 2013.

[8] Y.-X. Jiang, J.-X. Yin, M. M. Denner, N. Shumiya, B. R. Ortiz, G. Xu, Z. Guguchia, J. He, M. S. Hossain, X. Liu, J. Ruff, L. Kautzsch, S. S. Zhang, G. Chang, I. Belopolski, Q. Zhang, T. A. Cochran, D. Multer, M. Litskevich, Z.-J.

Cheng, X. P. Yang, Z. Wang, R. Thomale, T. Neupert, S. D. Wilson, and M. Z. Hasan, "Unconventional chiral charge order in kagome superconductor KV_3Sb_5," *Nature Materials*, vol. 20, pp. 1353–1357, 2021.

[9] H. Zhao, H. Li, B. R. Ortiz, S. M. L. Teicher, T. Park, M. Ye, Z. Wang, L. Balents, S. D. Wilson, and I. Zeljkovic, "Cascade of correlated electron states in the kagome superconductor CsV_3Sb_5," *Nature*, vol. 599, pp. 216–221, 2021.

[10] M. M. Denner, R. Thomale, and T. Neupert, "Analysis of charge order in the kagome metal AV_3Sb_5 ($A = \mathrm{K}, \mathrm{Rb}, \mathrm{Cs}$)," *Physical Review Letters*, vol. 127, article 217601, 2021.

[11] X. Feng, K. Jiang, Z. Wang, and J. Hu, "Chiral flux phase in the kagome superconductor AV_3Sb_5," *Science Bulletin*, vol. 66, pp. 1384–1388, 2021.

[12] M. Kang, S. Fang, J.-K. Kim, B. R. Ortiz, S. H. Ryu, J. Kim, J. Yoo, G. Sangiovanni, D. Di Sante, B.-G. Park, C. Jozwiak, A. Bostwick, E. Rotenberg, E. Kaxiras, S. D. Wilson, J.-H. Park, and R. Comin, "Twofold van Hove singularity and origin of charge order in topological kagome superconductor CsV_3Sb_5," *Nature Physics*, vol. 18, pp. 301–308, 2022.

[13] T. Park, M. Ye, and L. Balents, "Electronic instabilities of kagome metals: saddle points and Landau theory," *Physical Review B*, vol. 104, article 035142, 2021.

[14] Y.-P. Lin and R. M. Nandkishore, "Complex charge density waves at van Hove singularity on hexagonal lattices: Haldane-model phase diagrams and potential realization in the kagome metals AV_3Sb_5," *Physical Review B*, vol. 104, article 045122, 2021.

[15] T. Neupert, M. M. Denner, J.-X. Yin, R. Thomale, and M. Z. Hasan, "Charge order and superconductivity in kagome materials," *Nature Physics*, vol. 18, pp. 137–143, 2022.

[16] S. Zhou and Z. Wang, "Chern Fermi pocket, topological pair density wave, and charge-4e and charge-6e superconductivity in kagome superconductors," *Nature Communications*, vol. 13, article 7288, 2022.

[17] J. H. Jung, C.-H. Park, and J. Ihm, "A rigorous method of calculating exfoliation energies from first principles," *Nano Letters*, vol. 18, pp. 2759–2765, 2018.

[18] G. Kresse and J. Furthmuller, "Efficiency of ab-initio total energy calculations for metals and semiconductors using a plane-wave basis set," *Computational Materials Science*, vol. 6, pp. 15–50, 1996.

[19] G. Kresse and J. Furthmuller, "Efficient iterative schemes for ab initio total-energy calculations using a plane-wave basis set," *Physical Review B*, vol. 54, pp. 11169–11186, 1996.

[20] J. P. Perdew, K. Burke, and M. Ernzerhof, "Generalized gradient approximation made simple," *Physical Review Letters*, vol. 77, pp. 3865–3868, 1996.

[21] A. Togo and I. Tanaka, "First principles phonon calculations in materials science," *Scripta Materialia*, vol. 108, pp. 1–5, 2015.